Intersectional Monosynaptic Tracing for Dissecting Subtype-Specific Organization of GABAergic Interneuron Inputs

Michael J. Yetman[1], **Eric Washburn**[1], **Jung Ho Hyun**[2], **Fumitaka Osakada**[3,4], **Yasufumi Hayano**[1], **Hongkui Zeng**[5], **Edward M. Callaway**[3], **Hyung-Bae Kwon**[2,6], and **Hiroki Taniguchi**[1,7,*]

[1]Development and Function of Inhibitory Neural Circuits, Max Planck Florida Institute for Neuroscience, Jupiter, Florida 33458, USA

[2]Cellular Basis of Neural Circuit Plasticity, Max Planck Florida Institute for Neuroscience, Jupiter, Florida 33458, USA

[3]Systems Neurobiology Laboratory, The Salk Institute for Biological Studies, La Jolla, California 92037, USA

[4]Laboratory of Cellular Pharmacology, Nagoya University, Furocho, Aichi 464-8601, Japan

[5]Allen Institute for Brain Science, Seattle, Washington 98103, USA

[6]Max Planck Institute for Neurobiology, Martinstried 82152, Germany

[7]PRESTO, Japan Science and Technology Agency, Chiyodaku, Tokyo 102-0076, Japan

Abstract

Functionally and anatomically distinct cortical substructures such as areas or layers contain different principal neuron (PN) subtypes that generate output signals representing particular information. Various types of cortical inhibitory interneurons (INs) differentially but coordinately regulate PN activity. Despite a potential determinant for functional specialization of PN subtypes, the spatial organization of IN subtypes that innervate defined PN subtypes remains unknown. Here we develop a genetic strategy combining a recombinase-based intersectional labeling method and rabies viral monosynaptic tracing, which enables subtype-specific visualization of cortical IN

ensembles sending inputs to defined PN subtypes. Our approach reveals not only cardinal but also underrepresented connections between broad, non-overlapping IN subtypes and PNs. Furthermore, we demonstrate that distinct PN subtypes defined by areal or laminar positions display different organization of input IN subtypes. Our genetic strategy will facilitate understanding of the wiring and developmental principles of cortical inhibitory circuits at unparalleled levels.

Introduction

The cortex is organized into spatially segregated functional domains at different levels, such as areas, columns, and layers, which process distinct classes of information and cooperate to generate integrative signals. Functional specialization of these cortical substructures is likely attributable to anatomical specialization of neuronal circuits, which includes assembly of unique combinations of cell types, specific cellular deployment, and selective synaptic connections. Thus, disentangling circuit diagrams of individual cortical substructures is fundamental to understanding the structural basis of cortical functions.

One of the canonical circuit modules conserved across the cortex comprises an excitatory PN and multiple types of input inhibitory INs, which differ in physiology, morphology, connectivity, and gene expression (an IN-PN circuit) [1–3]. PNs in distinct cortical substructures likely generate specific output signals encoding particular information. Consistent with this notion, PN subtypes exhibit unique gene expression profiles [4] as well as specific features in dendritic morphology, remote axonal projection, and local input/output connectivity [2,4–6]. As local inhibitory inputs from individual IN subtypes differentially play a key role in balancing and shaping PN activity [1,3], the organization of IN subtypes in IN-PN circuits might be another determinant for functional specificity of PN subtypes. However, little is known about the spatial organization of IN subtypes innervating defined PN subtypes. A systematic *in vivo* anatomical study to address this issue has been hampered by technical limitations.

In past studies, a classical paired recording coupled with dye-filling has been used to address the morphology, physiology, subcellular synapse specificity, and connectivity of cortical INs [7–9]. Unbiased, large-scale profiling of cortical INs using this method has provided a comprehensive view of morphologically and physiologically defined cell types and their functional connectivity [10]. However, this approach is low-throughput: only a limited number of inputs to PNs can be examined at one time. In addition, the transection of axons during preparation of brain slices, which interrupts detection of functional connectivity, is inherent in this method. The more recent development of monosynaptic retrograde tracing assisted by rabies viruses (RVs) has enabled high-throughput input mapping *in vivo*, overcoming the weakness of electrophysiology-based mapping methods [11–15]. However, this strategy fails to differentiate between types of input neurons.

Parvalbumin (PV)-, somatostatin (SOM)-, and vasoactive intestinal polypeptide (VIP)-expressing INs are broad, non-overlapping IN subtypes that have been most extensively studied. PV-INs innervate the perisomatic compartment of PNs and control the gain of their activity while SOM-INs innervate PN dendrites and locally regulate dendritic computations [1–3,8,9,16]. VIP-INs primarily innervate other INs and are involved in disinhibition of PNs

[1–3,17–19] although a small fraction of VIP-INs also innervate PNs [8,10,19–21]. It has been shown that these canonical IN subtypes are differentially recruited during circuit operation and animal behavior [1,3,17,18,22,23]. Thus, they serve as a good model to examine the spatial organization of functionally distinct IN subtypes in IN-PN circuits. Here we develop a novel genetic strategy named intersectional monosynaptic tracing (iMT), combining a Cre/Flp-based intersectional labeling method [24,25] with RV-based retrograde monosynaptic tracing techniques [11] to efficiently and reliably label IN subtypes sending inputs to defined PN subtypes. We demonstrate that our genetic method captures canonical inhibitory inputs to PNs as well as underrepresented ones such as translaminar inputs from PV-INs and direct inputs from VIP-INs. Furthermore, our approach uncovers that INs of the same subtype are differentially organized in IN-PN circuits depending on areal or laminar identity of PNs. Thus, iMT will facilitate systematic dissection of wiring principles for cortical IN subtypes that are connected to defined PN subtypes at unparalleled levels.

Results

Basic principle of iMT

The Cre-LoxP-based homologous DNA recombination has been widely employed for cell type-specific gene expression. However, it is impossible to genetically engineer RVs for Cre-dependent conditional gene expression because they have single stranded RNA genomes, which are never converted to DNA during their replication [11]. To visualize IN subtypes that send inputs to starter PNs (Fig. 1a), we developed a novel genetic strategy combining the principle of RV-mediated monosynaptic tracing [11] with a Cre/Flp recombinase-dependent intersectional labeling method [12,25]. TVA (a cognate receptor for EnvA) and RG (an RV envelope glycoprotein that is necessary for production and transsynaptic propagation of RVs) with YFP- or HA-tagged H2B (H2BYFP or HAH2B) (together referred as starter genes hereafter) are introduced into PNs in mice with a Cre/Flp-dependent dual RFP reporter [Ai65: *frt-stop-frt-loxP-stop-loxP-RFP* (*FSF-LSL-RFP*)] [25] and a Cre gene inserted into an IN subtype-specific gene locus (e.g. *PV-Cre, SOM-Cre*, and *VIP-Cre*) [24,26]. Layer 2/3 (L2/3) PNs (supragranular PNs) and L5/6 PNs (infragranular PNs) are preferentially transfected with starter genes by *in utero* electroporation (IUE) at embryonic day 15.5 (E15.5)/E16 and E12.5, respectively. EnvA-pseudotyped, RG-deleted RVs containing *CFP* and *Flp* genes (*EnvA-RVdRG-Flp-CFP*, *RV-Flp-CFP* hereafter) are then injected into brains of electroporated animals. Because TVA is not expressed in mammals, selective initial infection with EnvA-pseudotyped RVs occurs only in TVA-expressing starter PNs. As RG-deleted RVs can be replicated in and transsynaptically transported from only starter PNs that are exogenously complemented with RG, their spread is monosynaptically restricted. Under this condition, only INs of a target subtype that send direct inputs to starter PNs coexpress Cre and Flp, resulting in subtype-specific input labeling with RFP driven from a dual RFP reporter (Fig. 1b,c). Thus, target input INs express both RFP and CFP whereas non-target input neurons express only CFP (Fig. 1b) (all mouse lines, plasmids, and viruses are listed in Supplementary Table 1).

Specificity and efficiency of iMT

We first established retrograde monosynaptic tracing targeting supragranular PNs in the somatosensory cortex (SSC) as starter neurons because these PNs are easily targeted by IUE. We introduced multicistronic expression vectors containing starter genes (H2BYFP/TVA/RG) into supragranular PNs in wild type (WT) mice by IUE at E15.5 [27] (Supplementary Fig. 1a). The strong nuclear localized signals of H2BYFP indicate coexpression of TVA and RG and help to identify starter PNs. We injected *RV-Flp-CFP* viruses into brains at P21–30, which were analyzed after 6 days (P27–36) (Supplementary Fig. 1a). PNs expressing H2BYFP were largely localized in L2/3 (Supplementary Fig. 1b). Starter PNs that express both H2BYFP and CFP were predominantly found in L2/3 although a small number of CFP+/H2BYFP+ PNs were found in L4 (Supplementary Fig. 1b,e). The distribution of starter PNs in individual brains was similar (Supplementary Fig. 2a). It should be noted that this was also true of distinct groups of brains defined by different IUE time points (i.e. E12.5 and E16), which exhibit different spatial distributions of starter PNs from those with IUE at E15.5 (Supplementary Fig. 2; Supplementary Table 2,3; Chi-square test, p < 0.0001). Input neurons that express only CFP were distributed across all layers except L1 (Supplementary Fig. 1f). In addition, CFP+ neurons were found in the contralateral SSC and the thalamic area as expected from known long-range connectivity (Supplementary Fig. 1c,d). To validate the specificity of these observations, we performed several control experiments. First, we tested potential contamination by unpseudotyped RVs in our *RV-Flp-CFP* viral solution, which might cause TVA-independent non-specific infection [13]. We found no sign of contamination by unpseudotyped RVs because no CFP+ cells were observed when *RV-Flp-CFP* viruses were injected into WT brains lacking TVA expression (0 cells, 5 animals) (data not shown). Second, we examined RG dependency of RV spread in our experimental system. When RG was excluded from starter genes (Supplementary Fig. 1g), all CFP+ neurons were localized in L2/3 at the injection site and expressed H2BYFP (2064 cells, 3 animals) (Supplementary Fig. 1h-j), suggesting that transsynaptic RV spread from starter PNs to direct input neurons is tightly dependent on RG expression. These results confirm TVA-dependent initial RV infection and subsequent RG-dependent RV spread from starter PNs in our system. In addition, we found that the efficiency of local transsynaptic RV spread in our system (Single starter conditions: 30.4 ± 5.7 CFP+/H2BYFP- input neurons per CFP+/H2BYFP+ starter PN, 5 animals; Sparse starter conditions: 16.2 ± 0.9 CFP+/H2BYFP- input neurons per CFP+/H2BYFP+ starter PN, 5 animals) is comparable to previous studies as judged by the ratio of CFP+/H2BYFP- input neurons to CFP+/H2BYFP+ starter PNs in experiments with a similar number of starter PNs [15,28]. Together, we confirmed the specificity and efficiency of general input labeling in our retrograde monosynaptic tracing system.

We next performed pilot experiments to establish iMT that enables us to selectively visualize IN subtypes sending inputs to supragranular PNs in the SSC. We chose PV-INs as target inputs to supragranular PNs because they are the most abundant population within cortical INs [1,29], and the specificity of the method can be tested by immunohistochemistry with anti-PV antibodies. We injected *RV-Flp-CFP* viruses into brains of P21–30 dual RFP reporter mice with a *PV-Cre* allele electroporated with vectors containing starter genes (Fig. 2a). As expected many putative general inputs to supragranular PNs were labeled with CFP (Fig.

2b). A significant fraction of CFP+ neurons also expressed RFP (Fig. 2b). These RFP+/CFP + neurons are expected to be PV-INs sending inputs to supragranular PNs. Indeed, somata of starter PNs were surrounded by RFP+ basket-like bouton structures, which represent axonal terminals of PV-INs (Fig. 2c). Immunohistochemical analysis using anti-PV antibodies showed that more than 80% of RFP+ neurons express PV (83.9 ± 4.5 %, 300 cells, 3 animals) (Fig. 2d,f). Furthermore, we characterized the identity of RFP+ neurons by whole-cell patch clamp recording (Fig. 2g). When a step current was injected, fast and non-adaptive action potentials (APs) were triggered (Fig. 2h), confirming characteristics of PV+ basket cells (BCs) [1,3,10,30]. Additionally, the basic electrophysiological properties including resting membrane potential (RMP), AP threshold and duration, and input-output properties showed similarity to those of PV+ BCs [10,30] (Fig. 2i-l). These data suggest that iMT specifically detects PV-INs sending direct inputs to supragranular PNs.

To test the efficiency of intersectional labeling in our system, we examined what percentage of CFP+/PV+ neurons, which are expected to express both Cre and Flp, express RFP. We found that nearly all CFP+/PV+ neurons are RFP+ (95.9 ± 0.8%; 300 cells, 3 animals), confirming that CFP+/PV+ neurons express sufficient levels of Cre/Flp to remove stop cassettes by site-specific homologous recombination. Consistent with this result, we also found that almost all input CFP+ neurons infected with *RV-Flp-CFP* viruses express RFP in Flp-dependent RFP reporter mice that use the same frt-flanked stop cassettes as dual RFP reporter mice, directly verifying that the level of RV-derived Flp in CFP+ neurons is sufficient to excise stop cassettes (96.7 ± 0.3%; 300 cells, 3 animals) (Supplementary Fig. 3k,l). These results indicate that intersectional labeling in our system is highly efficient.

It should be noted that a fraction of RFP+ neurons expressed no CFP (14.5 ± 2.5%; 100 cells, 3 animals) (Fig. 2e,f). This is likely because input PV-INs transsynaptically receiving a small number of *RV-Flp-CFP* viral particles weakly expressed Flp and CFP but the level of CFP was under the limit of detection. Most of these RFP+/CFP- neurons were positive for PV (80.6 ± 2.8%; 100 cells, 3 animals). A similar observation was made when neurons sending inputs to L2/3 PNs were infected with *RV-Flp-CFP* viruses in Flp-dependent RFP reporter mice. We found that a small fraction of RFP+ neurons were RFP+/CFP- also in this condition (8.3 ± 2.0%; 300 cells, 3 animals). These results suggest that our system is slightly more efficient than the original RV tracing method, in which input visualization relies on fluorescent proteins expressed from RVs, in detecting input IN subtypes.

An unlikely but possible explanation for RFP expression in RFP+/PV- and RFP+/CFP- neurons is that RFP expression in dual RFP reporter mice is not tightly regulated by coexpression of Cre and Flp. Indeed, this was not the case because no RFP expression was induced in all negative control experiments where dual RFP reporter mice express Cre or Flp alone in the cortex (Supplementary Fig. 3a-j).

Taken together, these results suggest that iMT specifically and efficiently visualizes IN subtypes that send direct inputs to defined PNs.

Supragranular PNs in the SSC receive inputs from PV-INs across layers

In order to gain insight into the cellular/axonal organization of IN subtypes that innervate a defined population of PNs, we first analyzed PV-INs that send inputs to supragranular PNs in the SSC (Fig. 3a,e,f). We focused on the SSC as previous studies have provided plenty of information on basic anatomy and connectivity of PNs and INs in this area.

Although previous studies suggested that PV-INs predominantly innervate PNs in the same layer [31], we found input PV-INs across all layers except L1 (Fig. 3b-d). To quantitate the laminar distribution of these input PV-INs, we calculated the proportion of input PV-INs in each layer to total input PV-INs (Fig. 3g). A significant fraction of input PV-INs were localized in granular/infragranular layers. These results suggest that supragranular PNs receive not only local inputs from PV-INs in the same layer but also translaminar inputs from those in granular/infragranular layers.

The arrangement of IN axons approximately reflects the output organization of INs. To estimate the output organization of PV-INs that send inputs to supragranular PNs, we analyzed the laminar distribution of RFP+ neuronal processes. Although containing dendrites, a large portion of these processes is likely axons. We calculated the proportion of the area occupied by neuronal processes in each layer to the total area occupied by neuronal processes (Fig. 3h). We found biased localization of neuronal processes in L2/3 as well as L4 (Fig. 3b,h). These results suggest that at least a subpopulation of these input PV-INs heavily innervate granular neurons in addition to supragranular PNs.

Although a minor population, the presence of starter L4 PNs could change the interpretation of above results. To overcome this issue, we aimed to restrict starter PNs to supragranular layers by sparsely expressing starter genes (HAH2B/TVA/RG) in upper supragranular PNs with E16 IUE. For sparse expression of starter genes, we took advantage of residual recombinase activity of DreER; DreER retains weak recombinase activity even in the absence of Tamoxifen (Supplementary Fig. 4a). We optimized the concentration of Dre-dependent plasmids containing starter genes (HAH2B/TVA/RG) and DreER plasmids so that on average a few HAH2B+ PNs appear every 120 μm along the anteroposterior (A-P) axis in the electroporated area (Supplementary Fig. 4b-d). Under this condition, iMT with *RV-Flp-CFP* viruses gave rise to small clusters of CFP+ neurons, which were expected to contain CFP+/HAH2B+ starter PNs and RFP+ input PV-INs. We examined five isolated, small IN-PN circuit clusters, containing between 5 and 20 starter PNs (5 clusters, 5 animals) (Supplementary Fig. 5a-c) and between 31 and 115 input PV-INs (Supplementary Fig. 5d). As expected, starter PNs in these clusters were confined to supragranular layers and CFP+ input neurons were distributed across all layers except L1 (Supplementary Fig. 5e,f). In all cases, input PV-INs were found in all layers except L1 Supplementary Fig. 5g). The laminar distribution of processes and cell bodies of input PV-INs was substantially similar to that in the above experiments with dense CFP+/H2BYFP+ starter PNs (compare Supplementary Fig. 5g,h to Fig. 3g,h). These results suggest that even though a small number of starter L4 PNs are included, the above iMT with dense CFP+/H2BYFP+ starter PNs largely represent the cellular/axonal organization of PV-INs sending inputs to supragranular PNs.

To accomplish higher resolution analysis of the output organization of IN subtypes that innervate defined PN types, we generated a Cre/Flp-dependent dual reporter line that allows for intersectional expression of Synaptophysin-YFP (SypYFP) fusion proteins, which are known to visualize presynaptic axonal terminals. We injected *RV-Flp-RFP* viruses into the SSC of dual SypYFP reporter mice with a *PV-Cre* allele, in which supragranular PNs were electroporated with plasmids containing starter genes (HAH2B/TVA/RG) (Fig. 3i,m,n).

SypYFP+ punctate signals were observed across cortical layers in a similar pattern to the above described RFP+ processes from input PV-INs (Fig. 3j,k). We often found complexes of SypYFP+ puncta surrounding RFP+/HAH2B+ starter PNs, indicating specific expression of SypYFP in PV-INs (Fig. 3l). We quantitated the proportion of the area occupied by SypYFP+ puncta in each layer to the total area occupied by SypYFP+ puncta (Fig. 3o). Consistent with our results of RFP+ processes, the vast majority of SypYFP+ puncta were found in L2/3 and L4. These results suggest that at least a subpopulation of PV-INs innervating supragranular PNs send presynaptic inputs preferentially to L2/3 and L4.

Taken together, iMT targeting a group of supragranular PNs as starter neurons provided a global view of the cellular and axonal/presynaptic organization of their input PV-INs.

A single supragranular PN in the SSC receives inputs from PV-INs in multiple layers

iMT targeting a defined group of PNs as starter neurons provided insight into the broad organization of IN subtypes in IN-PN circuits. However, this does not allow us to disentangle the organization of IN subtypes in a single IN-PN circuit module. To examine the organization of PV-INs sending inputs to a single supragranular PN in the SSC by iMT, we employed sparse expression of starter genes in PNs as described above (Fig. 4a). We further optimized the condition by changing the injection volume of RV solution and the concentration of Dre-dependent plasmids containing starter genes (HAH2B/TVA/RG) and DreER plasmids. Under the optimal condition, we obtained five isolated, tiny IN-PN circuit clusters, each of which contains a single starter PN. All starter PNs were confined to L2/3, and their average distance from the pial surface was roughly 200 μm (205.7 ± 20.6 μm, 5 starter PNs) (Fig. 4b). These five starter PNs received inputs from between 5 and 11 PV-INs (Average: 7.4 ± 1.2 input PV-INs per starter PN, 5 animals) (Fig. 4c-h). This convergence rate of inputs from PV-INs was much higher than that estimated from iMT targeting many PNs as starter neurons (1.2 ± 0.2 input PV-INs per starter PN, 5 animals), suggesting that a significant number of PN pairs share multiple input PV-INs.

Although data from iMT with multiple starter PNs show that a group of supragranular PNs receive both local and translaminar inputs from PV-INs, it remains elusive whether a single supragranular PN does so. To address this issue, we analyzed the laminar distribution of PV-INs sending inputs to a single supragranular PN. Although there was variation in a range of the laminar distribution of input PV-INs, all five single starter PNs received both local and translaminar inputs from PV-INs (Fig. 4c-h). These results suggest that convergent inputs from PV-INs in distinct layers are a common input motif in supragranular PNs.

In order to quantitatively characterize the spatial organization of these PV-INs sending inputs to a single PN, we mapped their positions relative to a PN in three dimensions. We

generated 3D reconstructions of the IN-PN circuits using confocal micrographs (Fig. 4d-h). The distances between a starter PN and input PV-INs ranged from 71 to 625 μm. However, the majority of cells were located within several hundred micrometers from their starter PN (216.5 ± 19.8 μm; 37 RFP cells, 5 clusters) (Supplementary Fig. 6).

Together, these results demonstrated that iMT targeting a single starter PN is powerful for dissecting the fine-scale organization of IN subtypes in an IN-PN circuit module, which may not be accessible with many starter PNs.

Granular/infragranular PNs in the SSC receive inputs primarily from local PV-INs

To gain insight into differences in the organization of PV-INs that innervate PNs in distinct layers, we next performed iMT targeting granular/infragranular PNs as starter neurons in the SSC. We performed iMT using mice that underwent E12.5 IUE of starter genes (H2BYFP/TVA/RG) (Fig. 5a). In these animals, the vast majority of CFP+/H2BYFP+ starter PNs were concentrated in infragranular layers (Fig. 5b,c,e) while CFP+/H2BYFP- input neurons resided in all layers except L1 (Fig. 5c,f).

Unlike iMT targeting supragranular PNs, in which only one third of input PV-INs are located in the same layers as starter PNs, the laminar distribution of input PV-INs in iMT targeting granular/infragranular PNs were dramatically biased to the same layers as starter PNs (Fig. 5c,d,g). We also found that the vast majority of processes of input PV-INs are localized in granular/infragranular layers (Fig. 5c,d,h). Interestingly, we noticed a gap between granular and infragranular layers in the area covered by RFP+ processes, suggesting that there are few translaminar processes between these layers (Fig. 5d). Together, these results suggest that PV-INs innervating granular/infragranular PNs locally project axons primarily within the same layer.

Additionally, we noticed that infragranular PV-INs innervating supragranular PNs seem to exhibit sparser local axons in the same layers (Fig. 3b,d,o) than those innervating infragranular PNs (Infragranular PV-INs innervating infragranular PNs: 5137 ± 432 pixels/soma, 3 animals; Infragranular PV-INs innervating supragranular PNs: 2394 ± 670 pixels/soma, 5 animals; Student's two-tailed t-test, $p < 0.05$) (Fig. 5d,h). These results suggest the possibility that two distinct PV-IN subpopulations may exist in infragranular layers.

Together, we demonstrated that iMT is applicable for comparing the organization of IN subtypes that send inputs to PNs in distinct layers.

Unique cellular/axonal organization of SOM-INs that innervate supragranular PNs in distinct cortical areas

SOM-INs display distinct physiological and connection properties from PV-INs [8–10,16,19]. A recent study showed that distinct layers in the SSC include different SOM-IN subtypes, which exhibit unique axonal distributions and behavior-relevant responses [22]. One of central questions we would like to address using iMT is whether PNs in distinct cortical areas establish different inhibitory circuit organization. If this is the case, area-specific PNs might receive inputs from different combinations or proportion of SOM-IN subtypes, which can be represented by distinct cellular/axonal organization of input SOM-INs. To test this

hypothesis and to prove that iMT works for different classes of IN subtypes from PV-INs, we applied iMT to SOM-INs sending inputs to supragranular PNs in the anterior SSC (aSSC) and the motor cortex (MC), which neighbor in the sensorimotor area (Fig. 6a-c,f-i). The specificity of iMT for SOM-INs was confirmed by immunohistochemistry; roughly 80% of RFP+ neurons exhibited immunofluorescence for SOM ($80.2 \pm 5.2\%$; 100 cells, 3 animals) (Supplementary Fig. 7a).

In the aSSC, input SOM-INs were located in all layers but L1 with a strong bias to granular/ infragranular layers in a similar pattern to previous studies that examined the whole population of SOM-INs [19,32] (Fig. 6d,j). Neuronal processes from input SOM-INs in the aSSC showed enrichment in granular/supragranular layers (Fig. 6d,k). In contrast, nearly 60 % of input SOM-INs are located in L2/3 in the MC (Fig. 6e,l). This number was significantly higher than that of the aSSC (MC: 58.4 ± 1.6 %; aSSC: 22.0 ± 3.3 %; 5 animals each; Student's two-tailed t-test, $p < 0.0001$). The laminar distribution of processes from input SOM-INs was also highly biased to L2/3 in the MC (Fig. 6m). This preferential axonal projection to L2/3 was significantly different from the axonal distribution of input SOM-INs in the aSSC, where the vast majority of processes were located in granular/infragranular layers (L2/3 RFP processes: MC: 81.0 ± 2.1 %; aSSC: 39.1 ± 2.9 %; Student's two-tailed t-test, $p < 0.0001$; 5 animals each). These areal differences were also confirmed by bin analysis (Supplementary Fig. 8g,h). These results suggest that distinct cortical areas have different organization of SOM-INs innervating supragranular PNs.

L1 targeting SOM-INs are known as Martinotti cells, which contribute to local computations at the apical tufts of dendrites of PNs [1,22,33]. To gain insight into the axonal organization of Martinotti cells in distinct cortical areas, we observed processes from input SOM-INs in L1 in the above preparations. Surprisingly, we found that their axonal density in L1 is strikingly different between the aSSC and the MC (Fig. 6d,e, lower panels). The value of the area occupied by the processes in L1 normalized to the number of input SOM-INs was significantly higher in the MC compared to the aSSC (MC: 0.16 ± 0.02, aSSC: 0.03 ± 0.004; Student's two-tailed t-test, $p < 0.001$; 5 animals each) (Fig. 6n). No L1 areal difference was observed when the whole population of SOM-INs was labeled with RFP in Cre-dependent RFP reporter mice with a *SOM-Cre* allele (Supplementary Fig. 9). These results suggest that L1 targeting Martinotti cells that innervate supragranular PNs are differentially organized in the aSSC and the MC.

Taken together, we demonstrated that iMT is able to detect areal differences in the organization of IN subtypes in IN-PN circuits.

Cellular/axonal organization of VIP-INs that innervate supragranular PNs in the SSC

VIP-INs compose a third largest IN subtype, which primarily innervate other interneurons to exert a disinhibitory effect on PNs [1,3]. Although a recent study showed that a minor fraction of VIP-INs also innervate PNs [8,10,19–21], their cellular/axonal organization in IN-PN circuits is largely unknown. To address this question, we applied iMT to VIP-INs that innervate supragranular PNs in the SSC (Fig. 7a,b,g,h).

We consistently obtained RFP+ neurons in infected animals, indicating that a certain fraction of VIP-INs directly innervate supragranular PNs in the SSC (Fig. 7c). We examined the specificity of iMT for VIP-INs using immunohistochemistry and found that roughly 70% of RFP+ showed immunofluorescent signals for VIP (70.3 ± 7.7%; 66 cells, 3 animals) (Supplementary Fig. 7b). This relatively lower colocalization rate compared to iMT for PV-INs and SOM-INs led us to be concerned about the sensitivity of VIP-antibodies. To overcome this potential problem, we performed fluorescent *in situ* hybridization (FISH) against *VIP* mRNAs. We found that all RFP+ neurons express FISH signals of *VIP* mRNAs (100%; 69 cells, 3 animals) (Supplementary Fig. 7c), confirming high specificity of iMT for VIP-INs.

The ratio of RFP+ input VIP-INs to CFP+ general input neurons was much lower than those of PV- and SOM-INs (PV-INs: 18.7 ± 3.9 %, 3,786 RFP+ of 21,793 CFP+ cells; SOM-INs: 9.7 ± 1.6 %, 2,166 RFP+ cells of 22,443 CFP+ cells; VIP: 0.6 ± 0.2%, 255 RFP+ cells of 41,050 CFP+ cells; one-way ANOVA, $p < 0.001$; 5 mice each), consistent with the idea that the vast majority of VIP-INs primarily innervate other classes of INs. Nearly all input VIP-INs were spatially confined to L2–4 with a bias to L2/3 (Fig. 7c,i). Their processes spanned all six layers with preferential localization in L4 (Fig. 7c,j). This wide distribution across all layers suggests that at least a fraction of VIP-INs innervating supragranular PNs project axons to multiple layers.

These input VIP-INs tended to exhibit relatively small cell bodies and bipolar or multipolar processes (Fig. 7d). We found that they often show basket-like structures containing axonal boutons (Fig. 7e,f). To determine what types of neurons are likely enwrapped by these structures, we stained brain sections containing RFP+ input VIP-INs with anti-NeuN and anti-GAD67 antibodies. We found that all of the basket-like structures colocalized with NeuN+ cell bodies, suggesting that these basket-like axon terminals innervate neurons (50 baskets, 3 animals) (Fig. 7e). However, none of baskets surrounded GAD67+ somata (50 baskets, 3 animals) (Fig. 7f). Considering that neocortical neurons consist of PNs and INs, these results suggest that basket-like structures exclusively innervate excitatory PNs.

Overall, these results provided strong evidence that iMT is sensitive enough to detect underrepresented input IN subtypes that innervate defined PN types.

Discussion

RV-mediated monosynaptic tracing has been widely employed in recent studies to examine local and long-range inputs to genetically defined starter neurons in several brain areas [11–13,15,34]. In the present study, we further extended this genetic method by conferring cell type specificity on input neuron labeling. We combined RV-based retrograde monosynaptic tracing with recombinase-mediated intersectional labeling to parse inputs from distinct IN subtypes to PN subtypes (Fig. 1). iMT provides several advantages over conventional RV-based monosynaptic tracing. First, direct visualization of input IN subtypes by iMT will facilitate the characterization of their physiological and genetic properties by targeted patch-clamp recording and RNA profiling, respectively. Second, as iMT genetically tags input IN subtypes with recombinases, any sensors and actuators for neuronal activity can be

specifically expressed in target IN subtypes using conditional mice and adeno-associated viruses (AAVs). However, functional application of iMT may need to await use of RVs with lower toxicity such as CVS-N2cdG [35] and self-inactivating rabies viruses (SiRVs) [36]. Nevertheless, our present study indicates potential application of iMT to functional dissection of IN-PN circuits. Third, the axonal/presynaptic organization of input IN subtypes can be analyzed as shown in this study. Recent studies have identified more selective IN subtypes with specific molecular markers. With generation of Cre driver lines targeting these genes, iMT will serve as a powerful approach for dissecting the organization and function of diverse IN subtypes in cortical microcircuits.

Our results demonstrate that PNs with distinct areal and laminar identity exhibit different cellular/axonal organization of input IN subtypes (Supplementary Fig. 10). This raises the possibility that functionally distinct PN subtypes, which could be determined by areal and laminar positions and remote projection targets [5,6,37–40], exhibit different organization of IN subtypes in IN-PN circuits. Selectively targeting more defined PNs as starter neurons in our genetic system may lead to findings of functionally relevant inhibitory local circuits. For example, retrograde tagging of PNs with different projections using AAV2-retro may help achieve this purpose [41].

Additionally, the developmental processes and mechanisms by which a unique set of IN subtypes is assembled to PNs are largely unknown. Our genetic strategy can be easily combined with functional manipulation in PNs, allowing us to address this issue. Recent evidence has suggested that the laminar identity of PNs control the synaptic number of PV-IN inputs [34]. It would be intriguing to examine whether reprogramming of PN identity changes assembly of IN subtypes in IN-PN circuits.

In summary, we developed a powerful genetic strategy to specifically label IN subtypes innervating defined PNs. This strategy can be applied to different brain regions beyond the cortex to understand cell type-specific input organization and will eventually help elucidate more detailed brain-wide circuit diagrams in health and disease.

Methods

All studies were approved by the Max Planck Florida Institute for Neuroscience Institutional Animal Care and Use Committee.

Mice

Homozygous Cre/Flp dual responsive *frt-STOP-frt (FSF)-loxP-STOP-loxP (LSL)-RFP* mice (*Ai65*) [25] were bred to homozygous *PV-ires-Cre*, *SOM-ires-Cre*, and *VIP-ires-Cre* knockin mice [24,26] to produce *PV-ires-Cre/+;Ai65/+, SOM-ires-Cre/+;Ai65/+*, and *VIP-ires-Cre/+;Ai65/+* mice. Homozygous *FSF-LSL-Synaptophysin-YFP (SypYFP)* mice were bred to homozygous *PV-ires-Cre* mice to produce *PV-ires-Cre/+;FSF-LSL-SypYFP/+* mice. Homozygous *LSL-RFP* mice (*Ai14*) [42] were bred to homozygous *SOM-ires-Cre* mice to produce *SOM-ires-Cre/+;Ai14/+* mice. Homozygous *PV-ires-Cre* mice were bred to mice homozygous for *Ai65* and heterozygous for *Dlx5/6-Flp* [43] to produce *PV-ires-Cre/+;Dlx5/6-Flp/+;Ai65/+* mice. Homozygous *FSF-RFP* mice were bred to Swiss Webster (SW) mice to

produce *FSF-RFP/+* mice. Wild-type SW mice were used for control experiments to test specificity of RV-mediated mono-transsynaptic tracing. *PV-ires-Cre, SOM-ires-Cre, VIP-ires-Cre, Ai65, Ai14, FSF-LSL-SypYFP, FSF-RFP*, and *Dlx5/6-Flp* mice were first backcrossed with SW mice at least three times and then maintained as homozygotes. Female mice with SW background were used for breeding. Both males and females were used for analyses.

Generation of *FSF-LSL-SypYFP* mouse line

The targeting construct containing Rosa homology arms, a CAG promoter, and a DNA sequence encoding SypYFP was generated by replacing a sequence for tdTomato in the *Ai65* (*RCFL-tdT*) vector with that for SypYFP. This *RCFL-SypYFP* targeting vector was linearized by KpnI and introduced into 129SVj/B6 F1 hybrid ES cells (V6.5). G418-resistant ES clones were screened by PCR for correct targeting at the Rosa locus. The correct targeting rate was 69%. Positive ES clones were used for tetraploid complementation to obtain male heterozygous mice following standard procedures. The FSF-LSL-SypYFP mouse line will be available from the Jackson Laboratory as JAX#032467.

Generation of *FSF-RFP* mouse line

To produce Flp-dependent RFP reporter mice, dual RFP reporter mice (*Ai65*) were crossed to *E2A-Cre* mice, which express Cre recombinase under the control of the adenovirus E2A promoter [44]. Because of potential mosaic expression of Cre from *E2A-Cre* alleles, germ line cells in offspring with both a Cre allele and an RFP reporter allele from this cross can have two different genotypes: *E2A-Cre/+;FSF-RFP/+* and *E2A-Cre/+;FSF-LSL-RFP/+*. These offspring were further bred to SW mice to isolate *FSF-RFP/+* mice that contain no Cre. Following primers were used to detect *E2A-Cre* alleles and RFP reporter alleles and confirm the lack of *LSL* cassettes. (Cre Forward: 5'-CGGTCGATGCAACGAGTGATG-3', Cre Reverse: 5'-AGCCTGTTTTGCACGTTCACC-3'; ROSA Forward: 5'-CCCAAAGTCGCTCTGAGTTGTTATC'3', ROSA Mutant Reverse: 5'-GAAGGAGCGGGAGAAATGGATATG-3', ROSA WT Reverse: 5'-CCAGGCGGGCCATTTACCGTAAG-3'; LSL Forward: 5'-GAAAGCTTGCAGATCTGCGACTC-3', LSL-Reverse 5'-GATCAGCTTGATGGGGATCCAGAC-3').

In utero electroporation (IUE)

To predominantly target supragranular (L2/3) principal neurons (PNs) and granular (L4)/infragranular (L5/6) PNs, IUE was performed targeting cortical progenitors at embryonic day 15.5 (E15.5) and E12.5, respectively. To target upper supragranular PNs, IUE was performed at E16.0. This technique exclusively targets the ventricular zone of the pallium where PNs are produced and does not result in the electroporation of INs, whose progenitors reside in the medial ganglionic eminence of the subpallium. Plasmid DNAs diluted in PBS was injected into the cerebral ventricles using sharp pulled glass pipettes (~2 μl/embryo). For global expression of TVA and RG in PNs, embryos from timed, pregnant females were electroporated with either *pCAG-H2BYFP-2A-TVA-2A-RG* (E15.5 IUE: 1.5 μg/μl; E12.5 IUE: 2.5 μg/μl) or *pCAG-RSR-HAH2B-2A-TVA-2A-RG* (1.5 μg/μl)/*pCAG-Dre* (2.0 μg/μl) as previously described [27]. To achieve sparse expression of HAH2B, TVA and RG in PNs,

embryos were electroporated with *pCAG-RSR-HAH2B-2A-TVA-2A-RG* (2.5 μg/μl) and *pCAG-DreER* (0.05 μg/μl) at E16.0. Three different conditions of *pCAG-DreER* concentration (0.05 μg/μl, 0.1 μg/μl, and 0.25 μg/μl) were tested to optimize the sparse expression of HAH2B. To obtain single starter cells, *pCAG-RSR-HAH2B-2A-TVA-2A-RG* (3.0 μg/μl) and *pCAG-DreER* (0.02 μg/μl) were used at E16.0. The following conditions were used for electroporation at E15.5/E16.0 and E12.5: 2 poring pulses of 50 V followed by 5 pulses of 33 V and 5 pulses of 33 V, respectively (NEPA21 super electroporator, NEPA GENE).

Production of Rabies Viruses (RVs)

Cerulean fluorescent protein (CFP) and Flippase (Flp) were cloned into G-deleted rabies virus plasmids. The same was done for DsRed (RFP) and Flp. Unpseudotyped seed viruses were rescued from these plasmids as described previously [45]. Seed viruses were then expanded by sequential infections of B19G2 cells and pseudotyped with EnvA by infecting EnvA2 cells. Pseudotyped viruses were purified and titrated through the infection of HEK293T cells expressing TVA as described previously [46].

Virus injections

To infect supragranular PNs, five hundred nanoliters of *RV-Flp-CFP* or *RV-Flp-RFP* (5×10^8 viral particles/ml) was injected stereotaxically into superficial layers of the cortex on the left side of P21-P30 animals that had previously undergone IUE: the somatosensory cortex (SSC) (containing primarily barrel fields and minor trunk representations) (bregma: −1.0 mm; M-L: −3.0 mm; depth: −0.38 mm), the anterior SSC (aSSC) (containing primarily upper limb and minor barrel field representations) (bregma: 0.0 mm; M-L: −3.0 mm; depth: −0.38 mm), or the motor cortex (MC) (bregma: +1.5 mm; M-L: −1.0 mm; depth: −0.38 mm). To infect granular/infragranular PNs, the same amount of *RV-Flp-CFP* was injected into deep layers of the SSC (bregma: −0.5 mm; M-L: −3.0 mm; depth: −1.1 mm) on the left side of P21-P30 animals. In experiments to target single starter PNs, 50 nL instead of 500 nL of *RV-Flp-CFP* was injected into brains. After 6 days, the brains of animals were harvested as described below. For dense supragranular PN starter conditions, roughly half of resulting brains were useable for analysis. Infragranular starter PN and sparse starter PN conditions resulted in a success rate of approximately one in seven and one in three brains, respectively, due to more difficult E12.5 IUE and titration conditions, respectively.

Immunohistochemistry

Mice were perfused with saline and 4% PFA in pH 7.4 PBS. Brains were excised and postfixed in 2% paraformaldehyde overnight at 4°C. For three dimensional (3D)-reconstructions, brains with sparse infections were incubated in 10% gelatin in 50 mL conical vials at 37°C for 10 minutes to impregnate tissue with gelatin. The 10% gelatin together with the brains was then poured into plastic molds pre-incubated on ice. After 20 minutes on ice, gelatin blocks were removed from molds, cropped, and immersed in 4% PFA in pH 7.4 PBS for 4 hrs at 4°C. 60 μm thick sections were cut using an automated vibratome (Leica VT1200 S). All sections were blocked in 10% Normal Donkey Serum/0.1% Triton-X/PBS for 1 hr followed by overnight incubation with primary antibodies at 4°C in blocking solution, except in the case of anti-GAD67 staining where no Triton-X was used and

primary incubation was 48 hrs. After washing in PBS, sections were incubated with secondary antibodies in blocking solution for 2 hrs before washing and mounting in DAPI-containing media (DAPI Fluoromount-G, Southern Biotech, 0100–20).

The following primary antibodies were used in this study: rabbit polyclonal anti-RFP (1:800, Rockland, #600–401-379), chicken polyclonal anti-GFP (1:1000, Abcam, ab13970), guinea pig polyclonal anti-PV, (1:2000, Swant, PVG-213), rat monoclonal anti-SOM (1:250, Millipore, MAB354), rabbit polyclonal anti-VIP (1:500, Immunostar, #20077), mouse monoclonal anti-NeuN (1:500, Millipore, MAB377), mouse monoclonal anti-GAD67 (1:800, Millipore, MAB5406), and rat monoclonal anti-HA (1:500, Roche, #11–867-423–001). The following secondary antibodies were used: donkey antibodies conjugated to Alexa 488, Cy3, or Cy5 (Jackson ImmunoResearch, 150 µg/mL). For more detailed information, please refer to the Life Sciences Reporting Summary.

Fluorescent *in situ* hybridization (FISH)

FISH was performed as described previously [47] with slight modifications. Digoxigenin (DIG)-labeled single-strand riboprobe was synthesized using T7 RNA polymerase and DIG RNA labeling mix (Roche, #11277073910). The sequence of the RNA probe against VIP is 5'-

TTCTCTGATTTCAGCTCTGCCCAGAGGCCTCTTCCCATCATTTCTCCAGCTCTTCA AGAAAGTCTGCAGAATCTCCCTCACTGCTCCTCTTTCCATTCAGGATGGAGTTCAG GTATTTCTTCACAGCCATTTGCTTTCTGAGGCGGGTGTAGTTATCTGTGAAGACGG CATCAGAGTGTCGTTTGATTGGCACAGGATCTTCCGAGATGCTGCTGCTGATTCGT TTGCCAATGAGTGACTCAAGGTATTTTTTGGCAGAAATCTGACCCAGAAGTCTGC TGTAATCGCTGGTGAAAACTCCATCAGCATGCCTGGCATTTCTTGACACATCATAA TAGGGTGTGCCATTTTCTGCTAAGGGATTCTGCAAGATGTCAGAGTCTGCTTTTAA AGAGACTTGGTCAGGGTCACCTGCTCCTTCAAACGGCATCCTGTCATCCAGCCTA CTCACTACAGAAGGTGGTCCAAAGAGAGGCCAGGCCAGCGACTGAGAGAACAGC ACACTGAAGAGTATCAGGAATGCCAGG-3'. Sixty µm thick sections prepared from whole brains that underwent iMT for VIP-INs were treated with proteinase K (40 µg/ml for 30 min at room temperature) and hybridized at 63°C with DIG-labeled antisense riboprobes in a hybridization solution consisting of 40% formamide, 20 mM Tris-HCl (pH 7.5), 600 mM NaCl, 1 mM EDTA, 10% dextran sulfate, 200 mg/ml yeast tRNA, 1x Denhardt's solution. The sections were washed twice in 1x SSC (Invitrogen) containing 50% formamide and once in 0.1x SSC at 63°C, followed by 2 washes with 0.1 M maleic buffer (pH 7.5) containing 0.1% Tween 20 and 150 mM NaCl. Then, those sections were incubated with anti-DIG antibodies conjugated with alkaline phosphatase overnight at 4°C followed by 3 washes in PBST solution (PBS containing 0.3% Triton X-100). Sections were incubated with rabbit polyclonal anti-RFP antibodies overnight at 4°C. After washing 3 times in PBST, sections were incubated with biotinylated anti-rabbit IgG antibodies for overnight at 4°C followed by 3 washes in PBST. Those sections were incubated with Cy5-streptavidin (1:1000, Jackson ImmunoResearch, #016–170-084) to visualize RFP(+) cells for 2 hrs at room temperature. The native red fluorescent signals from RFP were completely bleached after this treatment. Color development for mRNA expression was performed in the presence of HNPP/FastRed solution (100 µg/ml HNPP, 250 µg/ml FastRed, Roche, #11758888001)

for 20 min at room temperature. The sections were washed 1 min in PBS and mounted with CC/Mount tissue mounting medium (Sigma, #C9368). Confocal images were taken immediately after color development.

Imaging

For quantification of the laminar distribution of somata, low magnification fluorescent images were captured using an epifluorescent microscope equipped with a CCD camera [BX51 (OLYMPUS), 4x UPLSAPO, NA: 0.16 (OLYMPUS)]. Z-stack images were acquired using a confocal microscope [CLSM 780 (ZEISS), 20x Plan ApoChromat, NA: 0.8 (ZEISS)].

Quantification

Laminar distribution of cell bodies—The laminar distribution of cell bodies of starter PNs (CFP+/H2BYFP+ or HAH2B+), general input neurons (CFP+/H2BYFP- or HAH2B-), and input interneuron (IN) subtypes (RFP+) were assessed using low magnification, epifluorescent images. DAPI nuclear staining was used to delineate the borders between L1, L2/3, L4, L5, and L6. The total number of neurons in each layer was counted within a 600 μm A-P (ten 60 μm sections) extent of the SSC or the MC, which has an RV injection site at the center, and divided by the sum of neurons in all layers to obtain the proportion of neurons in each layer.

Laminar distribution of neuronal processes and presynaptic terminals from input IN subtypes—Distribution of RFP positive processes from input IN subtypes was assessed by analyzing maximum intensity projection images generated from 20x confocal z-stack images that were taken from three adjacent sections near an RV injection site. Projection images were converted from RGB to 8-bit and the Triangle algorithm [48] was used to determine the brightness threshold. In this algorithm, a histogram of pixels ranked by brightness is constructed from the image. A line is then drawn from the brightness 'peak', where the maximum number of pixels reside, to the farthest end of the histogram, the point on the brightness scale where no pixels reside. The distance between this line and every point along the curve of the histogram is then computed, and the brightness value at which this distance is maximized is taken to be the brightness threshold for the image. After thresholding, the magic wand tool was then used to select and exclude soma RFP signal from the analysis. DAPI signal was used to determine cortical layers and the number of pixels representing RFP signals in each cortical layer was then calculated. These values were divided by the sum of pixels representing RFP signals in all layers, giving a 'percent RFP processes' value for each layer for that section. Finally, the average values of the three adjacent sections were used to obtain each animal's distribution of RFP processes. The laminar distribution of SypYFP signals was obtained using the same method.

In order to assess L1 innervation by SOM-INs that innervate supragranular PNs, we obtained the areas occupied by RFP positive processes in L1. This number was divided by the total number of RFP positive somata in that section. As above, this value was calculated for three adjacent sections, and these were averaged to obtain the L1 innervation index for that animal.

To assess the relative density of processes from infragranular RFP+ PV-INs innervating supragranular or infragranular PNs, we obtained the number of RFP+ pixels in infragranular layers and normalized to the number of infragranular RFP+ PV-INs in that section. As above, this value was calculated for three adjacent sections, and these were averaged.

Spatial binning method—Epifluorescent or confocal micrographs of coronal cortical sections were subdivided into spatial bins with 100 μm width. The proportion of starter cells, RFP+ input SOM-INs, and RFP+ processes from input SOM-INs in each bin was quantitated. In all cases, this method resulted in 11 full-size bins and a partial twelfth bin. These data were compared statistically, as described below.

Distance analysis for sparse samples—20x confocal Z-stack images were taken from gelatin embedded sections containing an IN-PN circuit module containing a single PN. These Z-stack images from between 3 and 4 adjacent 60 μm sections were concatenated using ImageJ software to form a complete but unaligned stack of all section containing RFP + neurons from sparse infections. Next, concatenated Z-stack TIF files were reoriented and aligned in BitPlane AutoAligner software by using at least three anatomical markers in the DAPI channel as a guide. The three-dimensional coordinates of all CFP+/HAH2B+ starter PNs and RFP+ PV-INs within these aligned, concatenated stacks were determined using the Spots tool in IMARIS software. From these three-dimensional coordinates, the distance between every RFP+ soma and CFP+/HAH2B+ starter PN was calculated. Distances were then divided into 100 μm bins to construct histograms of starter PN-to-PV-IN distances.

Electrophysiology

Ex vivo slice electrophysiology was performed on acute brain slices from mice at 6 days post viral injection. RFP fluorescence was used to perform guided whole-cell patch clamp recordings on infragranular input neurons.

The mice were anesthetized with isoflurane and rapidly decapitated. Brains were quickly removed and chilled in ice-cold high-magnesium cutting solution containing the followings (in mM): 100 Choline Chloride, 25 $NaHCO_3$, 2.5 KCl, 0.5 $CaCl_2$, 7 $MgCl_2$, 1.25 NaH_2PO_4, 25 glucose, 20 HEPES, 3.1 Na-pyruvate, 5 Na-ascorbate. pH and osmolarity were adjusted to 7.4 and ~300 mOsm, respectively. The isolated brain was glued onto the stage of a vibratome (Leica VT1000, Leica Biosystems, Buffalo Grove, IL, USA) and 300 μm-thick coronal slices were cut. The slices were transferred and incubated at 34°C for 30 min in a slice container superfused with artificial cerebrospinal fluid (ACSF) solution containing the followings (in mM): 124 NaCl, 26 $NaHCO_3$, 3.2 KCl, 2.5 $CaCl_2$, 1.3 $MgCl_2$, 1.25 NaH_2PO_4, 10 glucose, saturated with 95% O_2 and 5% CO_2 gas. Thereafter slices were maintained at room temperature for the experiments.

Whole-cell current-clamp recordings from somatosensory cortical cells were carried out at room temperature while the recording chamber was perfused with ACSF at 1–1.5 ml per min. The recordings were made using MultiClamp 700B amplifier controlled by Clampex 10.2 via Digidata 1440A data acquisition system (Molecular Devices, Sunnyvale, CA, USA). The pipette solution contained (in mM): 125 K-gluconate, 5 KCl, 10 Na2-phosphocreatine, 4 Mg-ATP, 0.4 Na- GTP, 10 HEPES, 1 EGTA, 3 Na-ascorbate (pH = 7.25

with KOH, 295 mOsm). After forming a whole-cell patch on the cell soma, the average value of resting membrane potential (RMP) was recorded at 63.2 ± 0.8 mV. Under this condition, intrinsic properties and input-output relationship were monitored. Action potential (AP) threshold was determined at the point when the slope of voltage change is 20 V/s. AP duration was measured from one side to the other side of AP waveform crossing at 20 mV when only one or two APs were triggered by minimal current injection.

Statistical analysis

Data are presented as the mean ± SEM throughout experiments. No statistical methods were used to pre-determine sample sizes but our sample sizes are similar to those reports in previous publications [15]. Data distribution was assumed to be normal but this was not formally tested. Due to the nature of our experiments, data collection and analysis could not be performed blind to the conditions of the experiments. Likewise, randomization was not employed, but all animals in one IUEed litter were treated the same. No animals or data points were excluded from analysis. For more detailed information, please refer to the Life Sciences Reporting Summary.

Prism 6 software was used to perform Student's t-test and one-way ANOVA to test differences as appropriate. Chi-square test was performed using RStudio Version 1.1.453 (RStudio Team (2015) (https://www.R-project.org) and used to compare shapes of the histograms of spatially binned data, using the formula:

$$X^2 = \sum_{i=1}^{k} \frac{\left(\dfrac{u_i}{N_u} - \dfrac{v_i}{N_v}\right)^2}{\dfrac{u_i}{N_u^2} - \dfrac{v_i}{N_v^2}}$$

Where μ and ν are the two histograms that are being compared, k is the bin number and degrees of freedom, N_μ and N_ν are the total content for each histogram. P values less than 0.05 were considered significant. Statistical significance was presented in the text and figures in the following manner: $*p < 0.05$, $**p < 0.01$, $***p < 0.001$, and $****p < 0.0001$. See Supplementary Table 3 for details of statistical tests.

Data Availability Statement

The data that support the findings of this study are available from the corresponding author upon reasonable request.

Supplementary Material

Refer to Web version on PubMed Central for supplementary material.

Acknowledgements

References

1. Tremblay R, Lee S & Rudy B GABAergic Interneurons in the Neocortex: From Cellular Properties to Circuits. Neuron 91, 260–292, doi:10.1016/j.neuron.2016.06.033 (2016). [PubMed: 27477017]

2. Huang ZJ Toward a genetic dissection of cortical circuits in the mouse. Neuron 83, 1284–1302, doi: 10.1016/j.neuron.2014.08.041 (2014). [PubMed: 25233312]

3. Kepecs A & Fishell G Interneuron cell types are fit to function. Nature 505, 318–326, doi:10.1038/ nature12983 (2014). [PubMed: 24429630]

4. Greig LC, Woodworth MB, Galazo MJ, Padmanabhan H & Macklis JD Molecular logic of neocortical projection neuron specification, development and diversity. Nat Rev Neurosci 14, 755–769, doi:10.1038/nrn3586 (2013). [PubMed: 24105342]

5. Harris KD & Shepherd GM The neocortical circuit: themes and variations. Nat Neurosci 18, 170–181, doi:10.1038/nn.3917 (2015). [PubMed: 25622573]

6. Krook-Magnuson E, Varga C, Lee SH & Soltesz I New dimensions of interneuronal specialization unmasked by principal cell heterogeneity. Trends Neurosci 35, 175–184, doi:10.1016/j.tins. 2011.10.005 (2012). [PubMed: 22119146]

7. Martin KA, Somogyi P & Whitteridge D Physiological and morphological properties of identified basket cells in the cat's visual cortex. Exp Brain Res 50, 193–200 (1983). [PubMed: 6641854]

8. Kawaguchi Y & Kubota Y Physiological and morphological identification of somatostatin- or vasoactive intestinal polypeptide-containing cells among GABAergic cell subtypes in rat frontal cortex. J Neurosci 16, 2701–2715 (1996). [PubMed: 8786446]

9. Kawaguchi Y & Kubota Y GABAergic cell subtypes and their synaptic connections in rat frontal cortex. Cereb Cortex 7, 476–486 (1997). [PubMed: 9276173]

10. Jiang X et al. Principles of connectivity among morphologically defined cell types in adult neocortex. Science 350, aac9462, doi:10.1126/science.aac9462 (2015). [PubMed: 26612957]

11. Wickersham IR et al. Monosynaptic restriction of transsynaptic tracing from single, genetically targeted neurons. Neuron 53, 639–647, doi:10.1016/j.neuron.2007.01.033 (2007). [PubMed: 17329205]

12. Miyamichi K et al. Cortical representations of olfactory input by trans-synaptic tracing. Nature 472, 191–196, doi:10.1038/nature09714 (2011). [PubMed: 21179085]

13. Watabe-Uchida M, Zhu L, Ogawa SK, Vamanrao A & Uchida N Whole-brain mapping of direct inputs to midbrain dopamine neurons. Neuron 74, 858–873, doi:10.1016/j.neuron.2012.03.017 (2012). [PubMed: 22681690]

14. Kim EJ, Juavinett AL, Kyubwa EM, Jacobs MW & Callaway EM Three Types of Cortical Layer 5 Neurons That Differ in Brain-wide Connectivity and Function. Neuron 88, 1253–1267, doi: 10.1016/j.neuron.2015.11.002 (2015). [PubMed: 26671462]

15. DeNardo LA, Berns DS, DeLoach K & Luo L Connectivity of mouse somatosensory and prefrontal cortex examined with trans-synaptic tracing. Nat Neurosci 18, 1687–1697, doi: 10.1038/nn.4131 (2015). [PubMed: 26457553]

16. Di Cristo G et al. Subcellular domain-restricted GABAergic innervation in primary visual cortex in the absence of sensory and thalamic inputs. Nat Neurosci 7, 1184–1186, doi:10.1038/nn1334 (2004). [PubMed: 15475951]

17. Fu Y et al. A cortical circuit for gain control by behavioral state. Cell 156, 1139–1152, doi: 10.1016/j.cell.2014.01.050 (2014). [PubMed: 24630718]

18. Pi HJ et al. Cortical interneurons that specialize in disinhibitory control. Nature 503, 521–524, doi: 10.1038/nature12676 (2013). [PubMed: 24097352]

19. Pfeffer CK, Xue M, He M, Huang ZJ & Scanziani M Inhibition of inhibition in visual cortex: the logic of connections between molecularly distinct interneurons. Nat Neurosci 16, 1068–1076, doi: 10.1038/nn.3446 (2013). [PubMed: 23817549]

20. Zhou X, Rickmann M, Hafner G & Staiger JF Subcellular Targeting of VIP Boutons in Mouse Barrel Cortex is Layer-Dependent and not Restricted to Interneurons. Cereb Cortex 27, 5353–5368, doi:10.1093/cercor/bhx220 (2017). [PubMed: 28968722]

21. Garcia-Junco-Clemente P et al. An inhibitory pull-push circuit in frontal cortex. Nat Neurosci 20, 389–392, doi:10.1038/nn.4483 (2017). [PubMed: 28114295]

22. Munoz W, Tremblay R, Levenstein D & Rudy B Layer-specific modulation of neocortical dendritic inhibition during active wakefulness. Science 355, 954–959, doi:10.1126/science.aag2599 (2017). [PubMed: 28254942]

23. Kvitsiani D et al. Distinct behavioural and network correlates of two interneuron types in prefrontal cortex. Nature 498, 363–366, doi:10.1038/nature12176 (2013). [PubMed: 23708967]

24. Taniguchi H et al. A resource of Cre driver lines for genetic targeting of GABAergic neurons in cerebral cortex. Neuron 71, 995–1013, doi:10.1016/j.neuron.2011.07.026 (2011). [PubMed: 21943598]

25. Madisen L et al. Transgenic mice for intersectional targeting of neural sensors and effectors with high specificity and performance. Neuron 85, 942–958, doi:10.1016/j.neuron.2015.02.022 (2015). [PubMed: 25741722]

26. Hippenmeyer S et al. A developmental switch in the response of DRG neurons to ETS transcription factor signaling. PLoS Biol 3, e159, doi:10.1371/journal.pbio.0030159 (2005). [PubMed: 15836427]

27. Saito T In vivo electroporation in the embryonic mouse central nervous system. Nat Protoc 1, 1552–1558, doi:10.1038/nprot.2006.276 (2006). [PubMed: 17406448]

28. Marshel JH, Mori T, Nielsen KJ & Callaway EM Targeting single neuronal networks for gene expression and cell labeling in vivo. Neuron 67, 562–574, doi:10.1016/j.neuron.2010.08.001 (2010). [PubMed: 20797534]

29. Rudy B, Fishell G, Lee S & Hjerling-Leffler J Three groups of interneurons account for nearly 100% of neocortical GABAergic neurons. Dev Neurobiol 71, 45–61, doi:10.1002/dneu.20853 (2011). [PubMed: 21154909]

30. Lazarus MS & Huang ZJ Distinct maturation profiles of perisomatic and dendritic targeting GABAergic interneurons in the mouse primary visual cortex during the critical period of ocular dominance plasticity. J Neurophysiol 106, 775–787, doi:10.1152/jn.00729.2010 (2011). [PubMed: 21613595]

31. Packer AM & Yuste R Dense, unspecific connectivity of neocortical parvalbumin-positive interneurons: a canonical microcircuit for inhibition? J Neurosci 31, 13260–13271, doi:10.1523/JNEUROSCI.3131-11.2011 (2011). [PubMed: 21917809]

32. Xu X, Roby KD & Callaway EM Immunochemical characterization of inhibitory mouse cortical neurons: three chemically distinct classes of inhibitory cells. J Comp Neurol 518, 389–404, doi:10.1002/cne.22229 (2010). [PubMed: 19950390]

33. Wang Y et al. Anatomical, physiological and molecular properties of Martinotti cells in the somatosensory cortex of the juvenile rat. J Physiol 561, 65–90, doi:10.1113/jphysiol.2004.073353 (2004). [PubMed: 15331670]

34. Chen SX, Kim AN, Peters AJ & Komiyama T Subtype-specific plasticity of inhibitory circuits in motor cortex during motor learning. Nat Neurosci 18, 1109–1115, doi:10.1038/nn.4049 (2015). [PubMed: 26098758]

35. Reardon TR et al. Rabies Virus CVS-N2c(DeltaG) Strain Enhances Retrograde Synaptic Transfer and Neuronal Viability. Neuron 89, 711–724, doi:10.1016/j.neuron.2016.01.004 (2016). [PubMed: 26804990]

36. Ciabatti E, Gonzalez-Rueda A, Mariotti L, Morgese F & Tripodi M Life-Long Genetic and Functional Access to Neural Circuits Using Self-Inactivating Rabies Virus. Cell 170, 382–392 e314, doi:10.1016/j.cell.2017.06.014 (2017). [PubMed: 28689641]

37. Brecht M Barrel cortex and whisker-mediated behaviors. Curr Opin Neurobiol 17, 408–416, doi:10.1016/j.conb.2007.07.008 (2007). [PubMed: 17702566]

38. Feldmeyer D Excitatory neuronal connectivity in the barrel cortex. Front Neuroanat 6, 24, doi:10.3389/fnana.2012.00024 (2012). [PubMed: 22798946]

39. Lindwall C, Fothergill T & Richards LJ Commissure formation in the mammalian forebrain. Curr Opin Neurobiol 17, 3–14, doi:10.1016/j.conb.2007.01.008 (2007). [PubMed: 17275286]

40. Molyneaux BJ, Arlotta P, Menezes JR & Macklis JD Neuronal subtype specification in the cerebral cortex. Nat Rev Neurosci 8, 427–437, doi:10.1038/nrn2151 (2007). [PubMed: 17514196]

41. Tervo DG et al. A Designer AAV Variant Permits Efficient Retrograde Access to Projection Neurons. Neuron 92, 372–382, doi:10.1016/j.neuron.2016.09.021 (2016). [PubMed: 27720486]

Methods-Only References

42. Madisen L et al. A robust and high-throughput Cre reporting and characterization system for the whole mouse brain. Nat Neurosci 13, 133–140, doi:10.1038/nn.2467 (2010). [PubMed: 20023653]

43. Miyoshi G et al. Genetic fate mapping reveals that the caudal ganglionic eminence produces a large and diverse population of superficial cortical interneurons. J Neurosci 30, 1582–1594, doi: 10.1523/JNEUROSCI.4515-09.2010 (2010). [PubMed: 20130169]

44. Lakso M et al. Efficient in vivo manipulation of mouse genomic sequences at the zygote stage. Proc Natl Acad Sci U S A 93, 5860–5865 (1996). [PubMed: 8650183]

45. Osakada F & Callaway EM Design and generation of recombinant rabies virus vectors. Nat Protoc 8, 1583–1601, doi:10.1038/nprot.2013.094 (2013). [PubMed: 23887178]

46. Wickersham IR, Sullivan HA & Seung HS Production of glycoprotein-deleted rabies viruses for monosynaptic tracing and high-level gene expression in neurons. Nat Protoc 5, 595–606, doi: 10.1038/nprot.2009.248 (2010). [PubMed: 20203674]

47. Watakabe A, Komatsu Y, Ohsawa S & Yamamori T Fluorescent in situ hybridization technique for cell type identification and characterization in the central nervous system. Methods 52, 367–374, doi:10.1016/j.ymeth.2010.07.003 (2010). [PubMed: 20637287]

48. Zack GW, Rogers WE & Latt SA Automatic measurement of sister chromatid exchange frequency. J Histochem Cytochem 25, 741–753, doi:10.1177/25.7.70454 (1977). [PubMed: 70454]
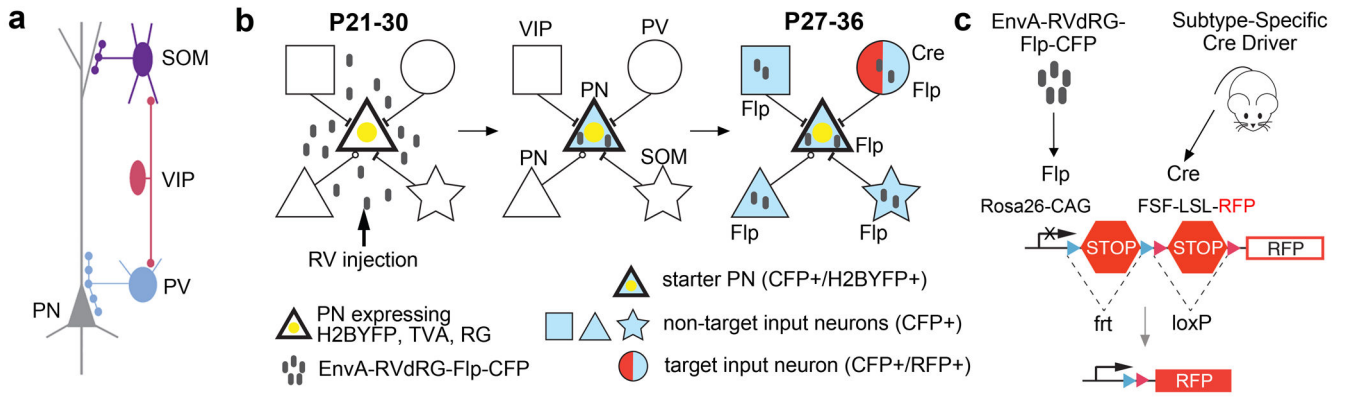
Figure 1.

iMT of cortical IN subtypes that send direct inputs to defined PNs.

(**a**) Canonical wiring diagram of three non-overlapping IN subtypes including PV-, SOM-, and VIP-INs.

(**b**) Schematic of iMT principle.

(**c**) Schematic of Cre/Flp-dependent RFP expression in dual reporter mice.
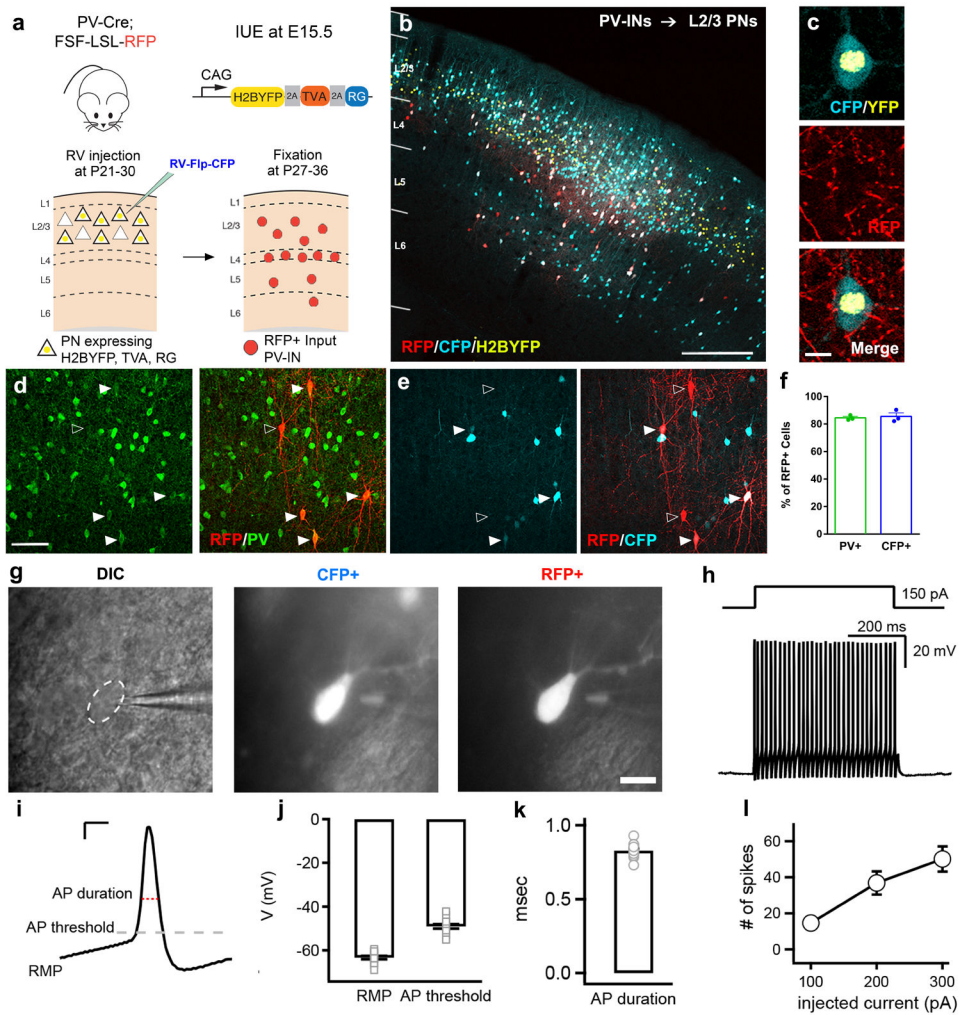
See also Supplementary Fig. 1.

Figure 2.

iMT specifically label PV-INs sending direct inputs to supragranular PNs.

(**a**) Experimental design for iMT of PV-INs sending direct inputs to supragranular PNs.

(**b**) Confocal projection image merging H2BYFP (yellow), CFP (cyan), and RFP (red) signals. CFP+/H2BYFP+, CFP+/H2BYFP-, and RFP+ neurons represent starter PNs, general input neurons, and putative input PV-INs, respectively. Scale bar, 500 μm.

(**c**) Merged and single channel images from a single confocal optical section of a CFP+/H2BYFP+ starter PN surrounded by basket-like structures from RFP+ putative PV-INs. Scale bar, 10 μm.

(**d,e**) Confocal projection images showing RFP+/PV+ and RFP+/PV- neurons (**d**) and RFP+/CFP+ and RFP+/CFP- neurons (**e**). Double and single positive neurons are indicated by closed and open arrowheads, respectively. Scale bar, 100 μm.

(**f**) Percentage of RFP+/PV+ and RFP+/CFP+ neurons to total RFP+ neurons (n = 3 animals).

(**g**) DIC and fluorescent images of an RFP+/CFP+ neuron in patch clamp configuration. Outline of putative PV-IN is shown in dotted white oval. Scale bar, 15 μm.

(**h**) Representative voltage trace from an RFP+ putative PV-IN given a 150 pA current injection for 500 ms.

(**i**) Sample AP trace showing definition of the resting membrane potential (RMP), AP threshold, and AP duration. Scale bar, 1 ms, 10 mV.

(**j**) RMP and AP threshold for RFP+ neurons (n = 13 RFP+ neurons, 4 animals).

(**k**) AP duration for RFP+ putative PV-INs (n = 13 RFP+ neurons, 4 animals).

(**l**) Spikes elicited from RFP+ putative PV-INs during 500 ms current injections (n = 13 RFP + neurons, 4 animals).

Data are presented as mean ± SEM. All experiments were repeated independently three (**b-f**) and four (**g-l**) times, respectively, with similar results.
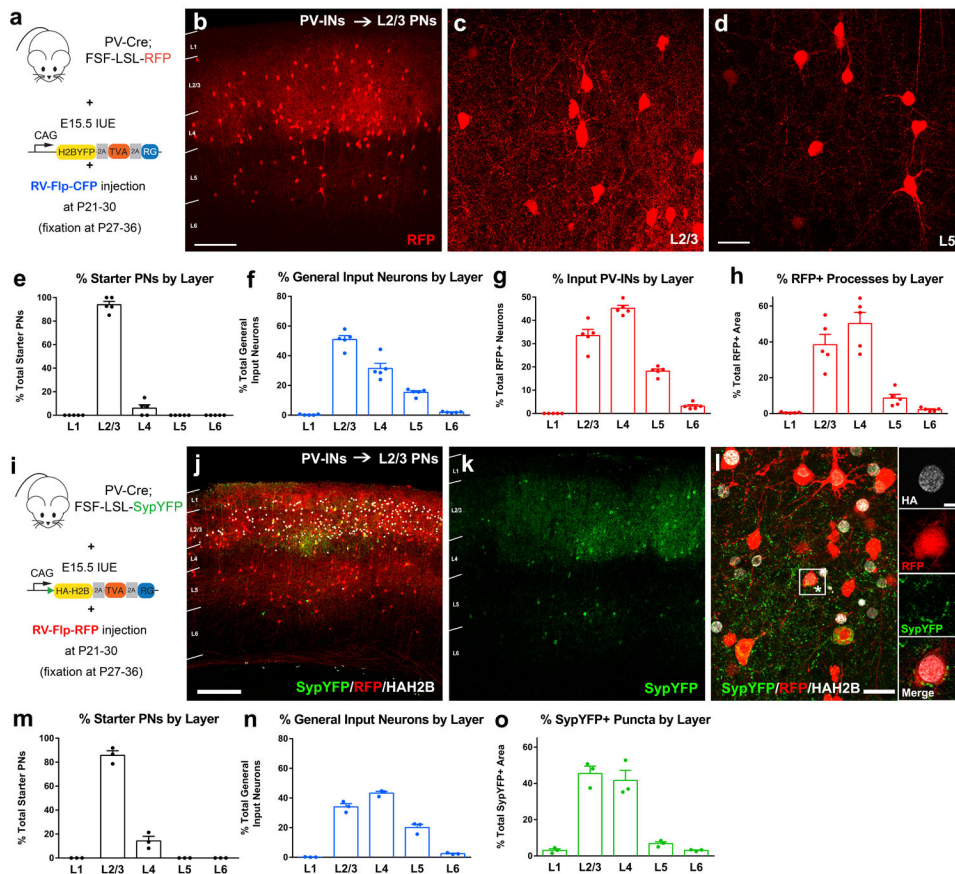
See also Supplementary Fig. 1,3.

Figure 3.

Supragranular PNs receive not only local but also translaminar inputs from PV-INs.

(**a**) Experimental design for iMT of PV-INs sending direct inputs to supragranular PNs.

(**b-d**) Confocal projection images of RFP+ PV-INs innervating supragranular PNs captured by iMT. Lower (**b**) and higher (L2/3 and L5 in **c** and **d**, respectively) magnification images of RFP+ input PV-INs. Scale bars, 200 μm (**b**), 50 μm (**c** and **d**).

(**e-h**) Laminar distribution of CFP+/H2BYFP+ starter PNs (**e**), CFP+/H2BYFP- general input neurons (**f**), RFP+ input PV-INs (**g**), and RFP+ processes (**h**) (n = 5 animals).

(**i**) Experimental design for iMT of PV-INs sending direct inputs to supragranular PNs using dual SypYFP reporter to visualize synaptic terminals.

(**j-l**) iMT of presynaptic terminals from PV-INs innervating supragranular PNs. Lower (**j** and **k**) and higher (**l**) magnification images. Merged (**j** and **l**) and single channel (**k**) confocal projection images. HAH2B (white), RFP (red), and SypYFP (green). Right small panels in **l** show merged and single channel images from a single confocal optical section, which is enlarged from a boxed area in a left panel. RFP+/HAH2B+ starter PN is surrounded by SypYFP puncta. Scale bars, 200 μm (**j** and **k**), 50 μm (left panel in **l**), 10 μm (right panels in **l**).

(**m-o**) Laminar distribution of RFP+/HAH2B+ starter PNs (**m**), RFP+/HAH2B- general input neurons (**n**), and SypYFP+ puncta (**o**) (n = 5 animals).

Data are presented as mean ± SEM. All experiments were repeated independently five (**b-h**) or three (**j-o**) times with similar results.

See also Supplementary Fig. 5,2b,c,8a,b.

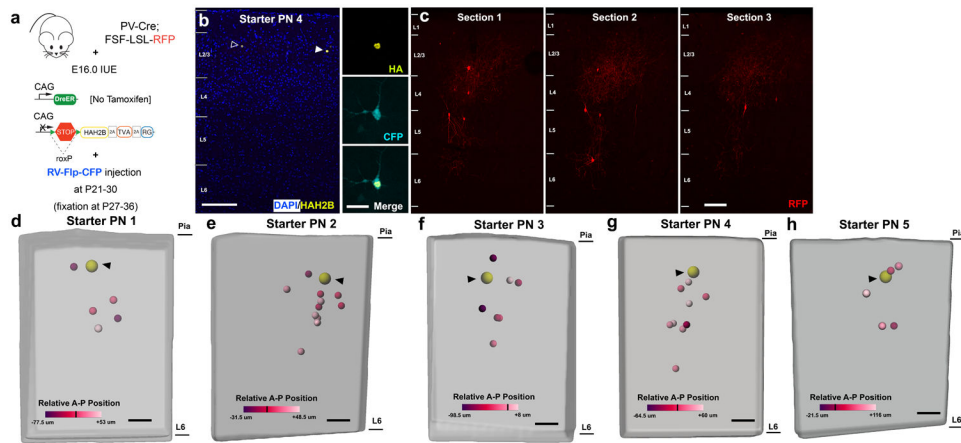See Supplementary Table 4,5 for numerical values.

Figure 4.

A single supragranular PN in the SSC receives inputs from PV-INs in multiple layers.

(**a**) Experimental design for iMT of PV-INs sending direct inputs to a single supragranular PN.

(**b,c**) iMT of input PV-INs innervating a single supragranular PN. Confocal projection image of HAH2B (yellow) and DAPI (blue) signals showing extremely sparse expression of HAH2B in supragranular PNs (**b**). Closed and open arrowheads represent an infected CFP+/HAH2B+ starter PN and a non-infected HAH2B+ PN, respectively. Small panels in **b** represent merged and single channel images from a single confocal optical section of a CFP+/HAH2B+ starter PN indicated by a closed arrowhead in left panel.

Confocal projection images of RFP+ input PV-INs (red) that send inputs to a single CFP+/HAH2B+ PN shown in **b**, which are distributed in serial, anterior-to-posterior 60 μm sections (**c**). Scale bars, 100 μm (**b,** left panel, and **c**) and 10 μm (**b,** right panels).

(**d-h**) 3-D reconstruction of IN-PN circuit modules, each of which contains a single starter PN (yellow sphere) and RFP+ input PV-INs (purple-white spheres). A-P positions of RFP+ input PV-INs relative to a starter PN are indicated by purple-to-white heatmap colors ranging from −98.5 to +116 μm. Scale bars, 100 μm. All experiments were repeated independently five times with similar results.
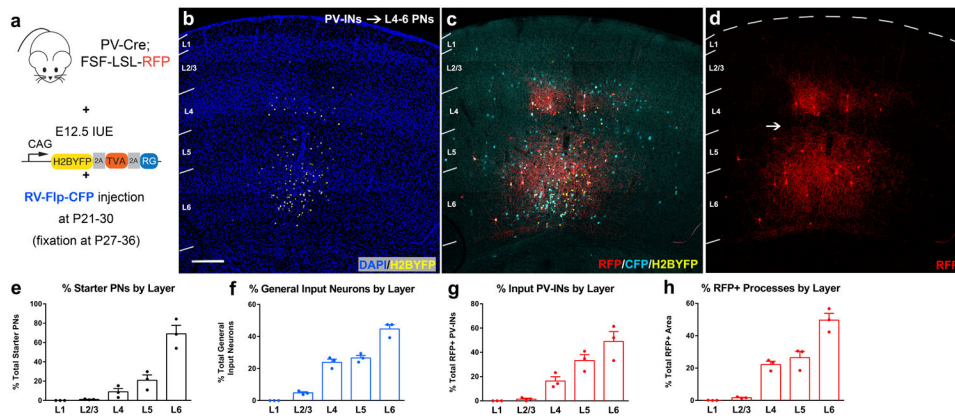
See also Supplementary Fig. 4,6.

Figure 5.

Granular/infragranular PNs receive local inputs from granular/infragranular PV-INs.

(**a**) Experimental design for iMT of PV-INs sending direct inputs to granular/infragranular PNs.

(**b-d**) iMT of PV-INs sending direct inputs to granular/infragranular PNs. Merged (**b** and **c**) and single channel (**d**) confocal projection images. DAPI (blue), H2BYFP (yellow), CFP (cyan), and RFP (red). CFP+/H2BYFP+, CFP+/H2BYFP-, and RFP+ neurons represent starter PNs, general input neurons, and input PV-INs, respectively. Scale bar, 200 μm.

(**e-h**) Laminar distribution of CFP+/H2BYFP+ starter PNs (**e**), CFP+/H2BYFP- general input neurons (**f**), RFP+ input PV-INs (**g**), and RFP+ processes (**h**) (n = 3 animals). Data are presented as mean ± SEM. All experiments were repeated independently three times with similar results.

See also Supplementary Fig. 2e,8c.

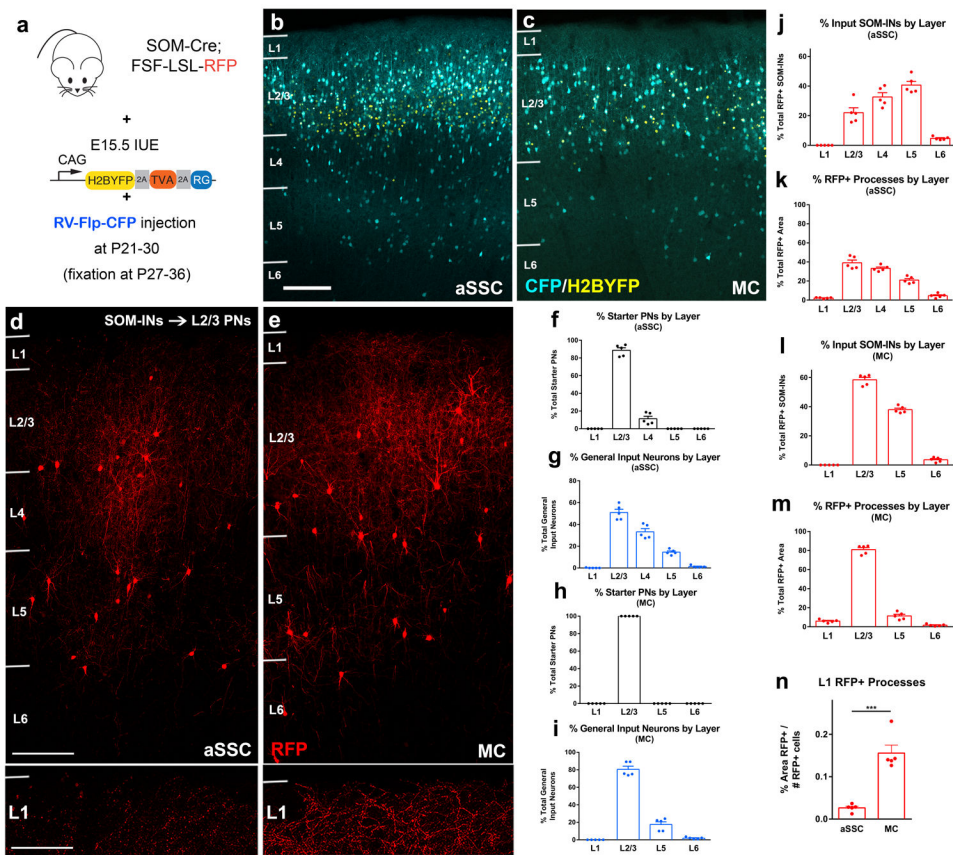See Supplementary Table 6,7 for numerical values.

Figure 6.

Unique cellular/axonal organization of SOM-INs that innervate supragranular PNs in distinct cortical areas.

(**a**) Experimental design for iMT of SOM-INs sending direct inputs to supragranular PNs.

(**b,c**) Confocal projection images merging H2BYFP (yellow) and CFP (cyan) in the aSSC (**b**) and the MC (**c**). CFP+/H2BYFP+ and CFP+/H2BYFP- represent starter PNs and general input neurons, respectively. Scale bar, 200 μm.

(**d,e**) Confocal projection images of RFP+ input SOM-INs (red) sending inputs to supragranular PNs in the aSSC (**d**) and the MC (**e**). Somata and axons in all layers (upper panels) and L1 axons (lower panels) of RFP+ input SOM-INs. Scale bars, 200 μm (upper panels), 20 μm (lower panels).

(**f-m**) Laminar distribution of CFP+/H2BYFP+ starter PNs (**f,h**), CFP+/H2BYFP- general input neurons (**g,i**), RFP+ SOM-INs (**j,l**), and RFP+ processes (**k,m**) in aSSC (**f,h,j,l**) and MC (**g,i,k,m**), respectively (n = 5 animals).

(**n**) Area occupied by L1 RFP+ processes normalized to the number of RFP+ somata in the aSSC and the MC (n = 5 animals).

Data are presented as mean ± SEM. All experiments were repeated independently five times with similar results.

See also Supplementary Fig. 2f,g,7a,8d,e,g,h,9.

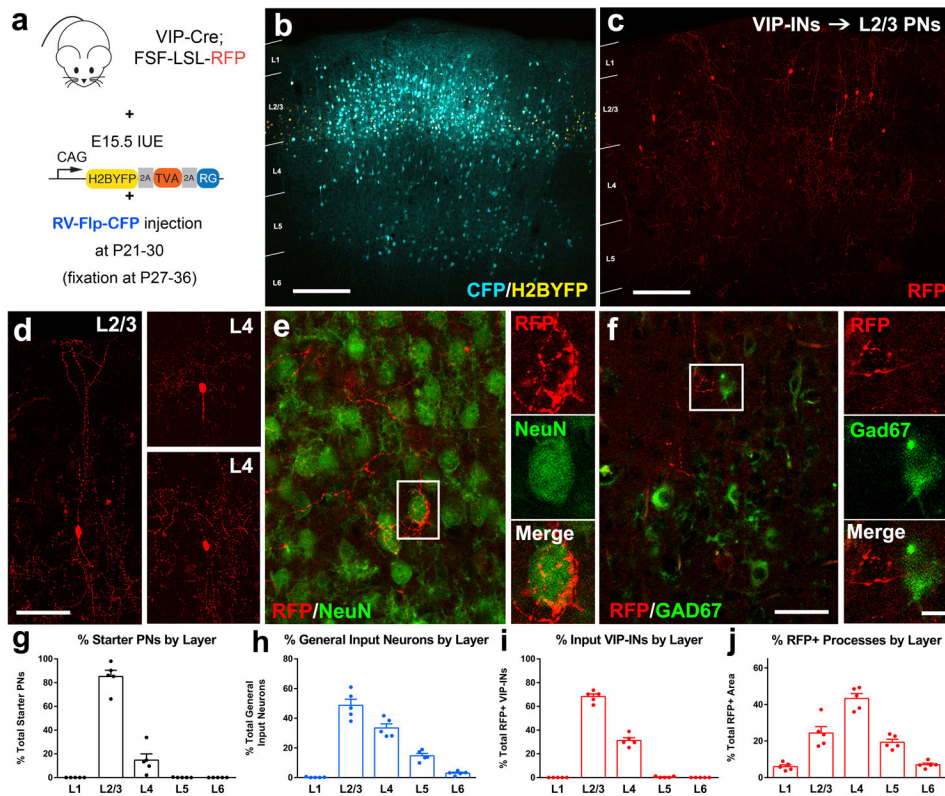See Supplementary Table 3,8,9 for numerical values and statistics.

Figure 7.
Cellular/axonal organization of VIP-INs that innervate supragranular PNs in the SSC.
(**a**) Experimental design for iMT of VIP-INs sending direct inputs to supragranular PNs.
(**b**) Confocal projection image merging H2BYFP (yellow) and CFP (cyan). CFP+/H2BYFP
+ and CFP+/H2BYFP- represent starter PNs and general input neurons respectively. Scale
bar, 200 μm.
(**c,d**) iMT of VIP-INs sending direct inputs to supragranular PNs in the SSC. Confocal
projection image showing RFP+ input VIP-INs (red) at lower magnification (**c**). Higher
magnification images of individual RFP+ input VIP-INs with bipolar and multipolar
morphologies in L2/3 and L4, respectively (**d**). Scale bars, 200 μm (**c**), 50 μm (**d**).
(**e,f**) Merged confocal projection images of RFP+ basket-like axonal terminals from input
VIP-INs (red) and NeuN or Gad67 (green) in **e** and **f**, respectively. Right small panels in **e**
and **f** represent merged and single-channel images from a single confocal optical section,
which is enlarged from a boxed area in left panels. Scale bars, 50 μm (left panels), 10 μm
(right panels).
(**g-j**) Laminar distribution of CFP+/H2BYFP+ starter PNs (**g**), CFP+/H2BYFP- general
input neurons (**h**), RFP+ input VIP-INs (**i**), and RFP+ processes (**j**) (n = 5 animals).
Data are presented as mean ± SEM. All experiments were repeated independently five times
with similar results.
See also Supplementary Fig. 2h,7b,c,8f.
See Supplementary Table 10,11 for numerical values.